Magnetoelectroelastic control of magnetism in an artificial multiferroic

J. Heidler,[1,2] M. Fechner,[3] R. V. Chopdekar,[1,4,5,*] C. Piamonteze,[1,†] J. Dreiser,[1] C. A. Jenkins,[6] E. Arenholz,[6]
S. Rusponi,[7] H. Brune,[7] N. A. Spaldin,[3] and F. Nolting[1]

[1]*Swiss Light Source, Paul Scherrer Institut, 5232 Villigen PSI, Switzerland*
[2]*SwissFEL, Paul Scherrer Institut, 5232 Villigen PSI, Switzerland*
[3]*Materials Theory, ETH Zürich, 8093 Zürich, Switzerland*
[4]*Laboratory for Micro- and Nanotechnology, Paul Scherrer Institut, 5232 Villigen, Switzerland*
[5]*Department of Chemical Engineering and Materials Science, University of California-Davis, Davis, California 95616, USA*
[6]*Advanced Light Source, Lawrence Berkeley National Laboratory, Berkeley, California 94720, USA*
[7]*École Polytechnique Fédérale de Lausanne, Institute of Physics, 1015 Lausanne, Switzerland*
(Received 9 September 2015; revised manuscript received 16 June 2016; published 5 July 2016)

We study the coexistence of strain- and charge-mediated magnetoelectric coupling in a cobalt (0–7 nm) wedge on ferroelectric (011)-oriented $[Pb(Mg_{1/3}/Nb_{2/3})O_3]_{0.68}$-$[PbTiO_3]_{0.32}$ using surface-sensitive x-ray magnetic circular dichroism spectroscopy at the Co $L_{3,2}$ edges. Three distinct electric field driven remanent magnetization states can be set in the Co film at room temperature. *Ab initio* density functional theory calculations unravel the relative contributions of both strain and charge to the observed magnetic anisotropy changes illustrating *magnetoelectroelastic* coupling at artificial multiferroic interfaces.

Interface engineering is widely used to enhance or create new functionalities not present in the constituent materials, ranging from two-dimensional electron gases at insulating oxide interfaces [1] to exchange bias [2]. This approach is also employed to create and/or enhance the magnetoelectric (ME) coupling in designed/artificial multilayered multiferroics. The possibility of controlling magnetism by an electric field is technologically very attractive and it highlights intriguing physical phenomena underlying the interfacial coupling mechanisms. Starting with the electric field effect at the interface between ferromagnets and dielectrics [3–5] to induce changes of magnetic anisotropy, the advent of multiferroics by design brought the possibility of imprinting changes in the ferromagnet in a nonvolatile way [6]. Coupling schemes include the strain transfer from a piezoelectric to a ferromagnetic thin film which allows manipulating magnetic properties throughout the film thickness [7–14]. More spatially limited effects include charge doping of a complex oxide which creates a significant magnetic reconstruction within the screening length of the interface [15–17] or a change in exchange coupling at the interface for different ferroelectric polarizations [18,19]. Other effects such as the control of exchange bias [20,21] or the tuning of domain wall motion [22] by ME coupling were also employed. Multiferroic junctions with four logic states illustrate the high degree of tunability of transport across ME interfaces [23–26]. The origin of the change in tunnel resistance with electric polarization lies in the ferromagnetic/ferroelectric (FM/FE) interface.

The coexistence of strain and charge effects have seldom been reported [27–30] and have so far been explained in a phenomenological framework. Such coexistence of coupling mechanisms opens up new possibilities for enhancement of the ME coupling. In this work we have studied the room-temperature ME coupling at the interface between a FM Co wedge film and the FE (011)-oriented $[Pb(Mg_{1/3}Nb_{2/3})O_3]_{0.68}$-$[PbTiO_3]_{0.32}$ (from here on PMN-PT) using x-ray magnetic circular dichroism (XMCD) to disentangle interface and bulk effects in a single system. We demonstrate how the coexistence of multiple mechanisms can be used to enhance the ME coupling as well as manipulate magnetic spin textures solely through the application of electric fields in a nonvolatile and reversible manner at room temperature. DFT calculations for different strain and charge states suggest a *magnetoelectroelastic* effect that induces a magnetic spiral through the Co film thickness.

Relaxor (011)-oriented FE $PMN_{(1−x)}$-PT_x, with a composition of $x = 0.32$ located in the morphotropic phase boundary region [31] (Atom Optics Co., LTD., Shanghai, China), is used as a substrate due to its strong piezoelectric properties. Its crystal structure is monoclinic with lattice constants $a = 4.02$ Å, $b = 4.01$ Å, and $c = 4.03$ Å [31]. A Co wedge with linearly increasing thickness from 0 to 7 nm is grown on (011)-oriented PMN-PT via thermal evaporation, with the substrate kept at room temperature. A 2 nm thick Cr capping layer was thermally evaporated to avoid oxidation of Co when exposed to air. A 30 nm Au film serves as bottom electrode. XMCD characterization shows that the Co film exhibits no magnetization at room temperature for nominal thicknesses below approximately 1.5 nm. This fact indicates a likely 3D Volmer-Weber growth mode, which can take place for depositions at room temperature due to limited surface diffusion of adatoms. X-ray diffraction measurements on the Co/PMN-PT bilayer showed that the Co thin film grows face centered cubic (fcc) textured with [111] for the OOP direction. The only observable peak using the Cu K_{α} line as source was at 44.35° corresponding to the 100% intensity peak of fcc Co, nominally at 44.2°. Other peaks, such as the 45% intensity (200) fcc peak at 51.58° or the 100% intensity (101) peak for hexagonal close packed Co at 47.46° were absent.

Figure 1(a) shows the sample design and measurement geometry. Depending on the electric field applied across (011)-oriented PMN-PT, three distinct remanent FE polarization

---

*Corresponding author: rchopdekar@ucdavis.edu
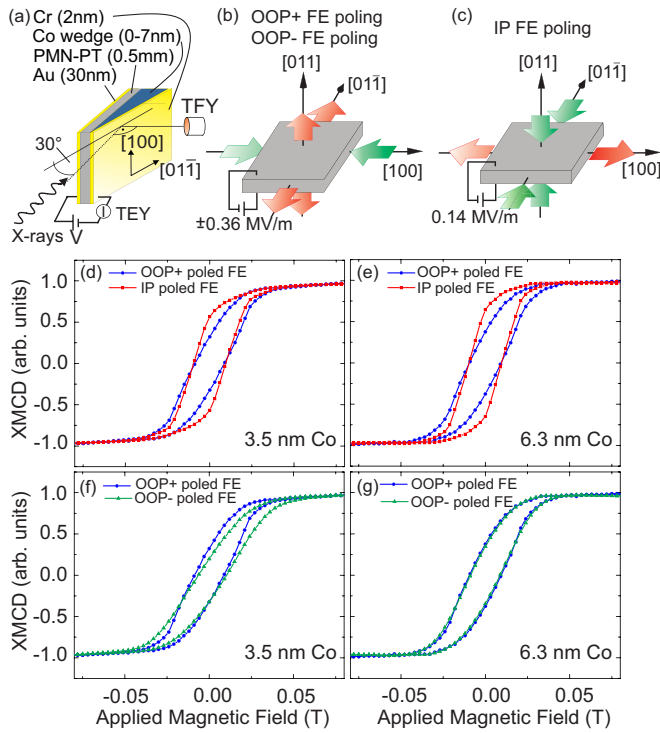†Corresponding author: cinthia.piamonteze@psi.ch

FIG. 1. (a) Measurement geometry. (b) and (c) Lattice parameter changes in OOP/IP poled PMN-PT, respectively. Green (red) arrows indicate compressive (tensile) strain in Co. (d)–(g) XMCD hysteresis curves probing the Co magnetization projection along the [01$\bar{1}$] PMN-PT crystal direction for the three distinct FE polarization states. (d) and (e) Switching the FE polarization from an OOP (blue curve) to an IP poled state (red curve) probing a nominal Co thickness of 3.5 nm (d) and 6.3 nm (e), induces an anisotropy change with higher remanent magnetization. (f) For 3.5 nm Co thickness, OOP poled polarization directions exhibit also different anisotropies. (g) For 6.3 nm Co thickness the anisotropy change for oppositely OOP poled FE is now absent.

states can be set. The FE polarization is poled positively or negatively out-of-plane (OOP+ or OOP−) by applying an electric field of ±0.36 MV/m at the bottom electrode, while the top electrode is connected to ground. When comparing OOP+ and OOP− poled FE no lattice parameter change in PMN-PT is expected and the Co top layer encounters identical strain conditions. However, FE polarization switching alters the interfacial charge that has to be screened by the adjacent cobalt layer through accumulation or depletion of electrons. Sweeping between opposite OOP FE polarization directions, (011)-oriented PMN-PT exhibits a remanent in-plane (IP) poled state at the coercive electric field (±0.14 MV/m). The switching from an OOP to an IP poled configuration and vice versa is accompanied by structural changes of the PMN-PT [14,32] as indicated in Figs. 1(b) and 1(c) that act on the Co top layer. OOP ↔ IP switching alters both the strained state of cobalt and the interfacial charge seen by the Co film. Note that both OOP poled states as well as the IP poled configuration are stable at remanence. The FE polarization

of (011)-oriented PMN-PT at 298 K was measured to be $2 \cdot \boldsymbol{P}_{\text{PMN-PT}} = 60 \ \mu\text{C/cm}^2$.

XMCD measurements at the Co $L_{3,2}$ edges were carried out at the X-Treme beamline [33] at the Swiss Light Source, Paul Scherrer Institut, Switzerland and at beamline 6.3.1 [34] at the Advanced Light Source, Lawrence Berkeley National Laboratory, California, USA. In XMCD, the absorption intensity difference between opposite light helicities is an element sensitive probe of magnetization along the photon propagation direction [35]. Spectra were recorded at room temperature with an incidence angle of 60° (angle between surface normal and x-rays incident direction), measuring the projected magnetization along the [01$\bar{1}$] crystal direction of the PMN-PT. The external magnetic field was applied along the x-ray beam direction.

Co XMCD hysteresis loops along the [01$\bar{1}$] direction, taken in total electron yield (TEY) mode for oppositely OOP poled states as well as the IP poled configuration at distinct thicknesses of the wedge, highlight two different ME coupling mechanisms at play. Electrical switching from an OOP poled to an IP poled state induces an anisotropy change with higher remanent magnetization as seen in Fig. 1(d) for a nominal Co thickness of 3.5 nm. The same behavior is observed probing a thicker part of the wedge at a nominal Co thickness of 6.3 nm in Fig. 1(e). Additionally we observe a more subtle anisotropy change comparing hysteresis curves taken for oppositely OOP poled FE in Fig. 1(f). This anisotropy change is not observed in the thicker part of the wedge, as seen by the nearly identical hysteresis loops of Fig. 1(g). TEY is a surface-sensitive detection mode where the probability of electron escape from the Co/PMN-PT interface decays exponentially with increasing Co top layer thickness (the electron sampling depth for Co is about 2.5 nm [36]). Therefore, the observed difference in magnetic anisotropy in Fig. 1(f) and its absence in Fig. 1(g) hints that its origin lies at the interface between Co and PMN-PT. As pointed out above, this effect cannot be attributed to a piezoelectric-magnetostrictive coupling since the strain transfer from the PMN-PT in the two states is equivalent. Hence, this anisotropy change due to the substrates' opposite OOP polarities suggests a charge driven magnetoelectric coupling. The anisotropy change shown in Figs. 1(d) and 1(e) at both the thinner and the thicker part of the wedge can be understood in terms of the magnetostriction of Co in response to the lattice parameter changes of PMN-PT [14]. Since strain is a "bulk" effect, its influence persists throughout the whole Co film thickness. For a quantitative analysis, a series of XMCD spectra was taken as a function of applied electric field on the thin part of the wedge at 3.5 nm Co thickness at magnetic remanence after saturation in 2 T in total fluorescence yield (TFY). Sum rule analysis [37,38] was used to extract the magnetic moment $m_{\text{tot}} = m_{\text{s,eff}} + m_{\text{orb}}$ projected along the [01$\bar{1}$] direction (for details, see Appendix A). The resulting dependence on the electric field is given in Fig. 2, where the gray curve links successive measurements. m_{tot} is strongest at the coercive electric field, where the FE polarization is rotated in-plane. Comparing measurements of oppositely poled FE, OOP− poled PMN-PT results in a smaller Co m_{tot} than OOP+ poled PMN-PT. Here m_{tot} depends solely on the FE polarization state that the PMN-PT has been set in, irrespective
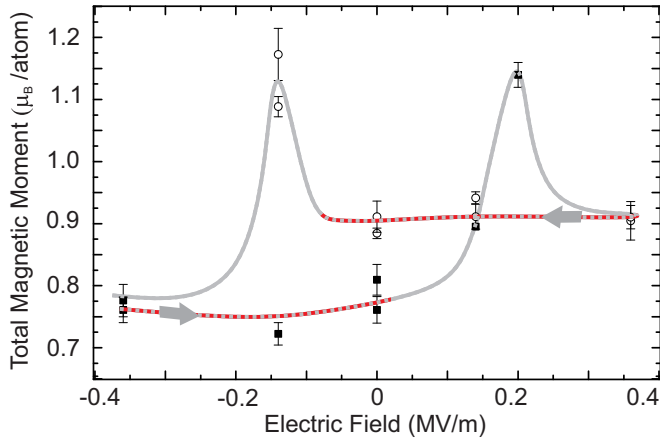
FIG. 2. Total magnetic moment (m_{tot}) along the [01$\bar{1}$] direction at remanence obtained from sum rule analysis as a function of applied electric field. The gray curve is a guide for the eye to link subsequent measurements. The arrow indicates the sweeping direction. Black squares (open circles) indicate measurements coming from OOP− (OOP+) poling. The dashed red branches highlight the dependence of m_{tot} on the FE OOP substrate polarity when switching between OOP+ and OOP−.

of an actively applied bias voltage. Note that in 2 T applied field no dependence of the saturation magnetization on the FE polarization can be observed. At 2 T field applied along the easy [100] direction, the effective spin moment $m_{s,eff} = 1.64 \pm 0.16 \, \mu_B$ and orbital moment $m_{orb} = 0.131 \pm 0.002 \, \mu_B$ compare well with literature values [39,40].

The impact of the FE order of PMN-PT on the electronic and atomic structure of a Co top layer is twofold. We observe a hysteretic behavior of remanent m_{tot} for OOP+ and OOP− poled FE suggesting a charge-driven magnetoelectric coupling contribution due to accumulation and depletion of electrons at the FM/FE interface. The contribution of charge to the change in total magnetic moment is highlighted by the dashed red branches in Fig. 2. Deviations occur only at the coercive electric field, where strain dominates while no net surface charge should be present. As the total moment at 2 T does not appreciably change with FE polarization but there is a significant change to m_{tot} at magnetic remanence, we attribute these changes in magnetization to changes in effective magnetic anisotropy energy (MAE) of the Co film. To investigate the separate influences of strain and screening charge on the MAE we perform first-principles DFT calculations of bulk fcc cobalt with each perturbation applied separately.

For Co films thicker than 1.5 nm [41–43], the shape anisotropy dominates the MAE and dictates an isotropic in-plane magnetization. This isotropy within the film plane is subsequently lifted by other MAE contributions. The bulk magnetocrystalline anisotropy for fcc Co favors an easy axis along the [111] and equivalent cubic directions. However, for a (111) film the strong shape anisotropy disfavors the low energy crystalline directions. Moreover, the volume magnetocrystalline anisotropy is isotropic within the (111) film plane and thus creates no anisotropy even if its magnitude is altered.

Another contribution to the MAE is magnetoelasticity, which exhibits lower order terms of the directional magnetization expansion [43] that are coupled to strain tensor elements (ϵ_{ij}). For cubic symmetry its energy contribution is

$$E_{mag-el} = B_1\left(\epsilon_{11}\alpha_1^2 + 2\epsilon_{22}\alpha_2^2 + \epsilon_{33}\alpha_3^2\right)$$
$$+ 2B_2(\epsilon_{23}\alpha_2\alpha_3 + \epsilon_{13}\alpha_1\alpha_3 + \epsilon_{12}\alpha_1\alpha_2),$$

where B_i are the cubic magnetoelastic constants and $\boldsymbol{\alpha}$ is the corresponding direction cosine of the magnetization. For the (111)-oriented fcc Co film we transform this expression [43] (see Appendix B) into hexagonal coordinates to yield, for the film plane magnetization:

$$E_{mag-el,hex}(\phi) = -\tfrac{1}{3}(B_1 + 2B_2)(\epsilon'_{100} - \epsilon'_{01\bar{1}})\sin^2(\phi), \quad (1)$$

where ϵ'_i are the strain elements in the film-plane labeled with respect to the PMN-PT substrate and ϕ is the angle of the in-plane magnetization relative to the [100] direction. The magnetoelasticity creates an easy in-plane direction which is determined by an "effective" magnetoelastic constant $B_{eff} = B_1 + 2B_2$.

By performing total energy calculations for a set of strained fcc-cobalt unit cells we compute B_1 and B_2 using DFT (see Appendix C). We find both $B_1 = -8.7 \, \text{MJ m}^{-3}$ and $B_2 = 7.2 \, \text{MJ m}^{-3}$ in reasonable agreement with experimental and theoretical literature values [43–45]. Moreover, the combination of these values gives a positive effective magnetoelastic constant B_{eff}. Consequently we predict that a net strain ($\epsilon'_{100} - \epsilon'_{01\bar{1}}) > 0$ creates an easy axis along the [01$\bar{1}$] direction, whereas ($\epsilon'_{100} - \epsilon'_{01\bar{1}}) < 0$ will produce an easy axis parallel to [100]. In PMN-PT, OOP → IP poling is accompanied by a strong positive ϵ'_{100} transferred to the Co film [32] resulting in a positive net strain. Hence, our theoretical finding is in agreement with the experimentally observed anisotropy change along [01$\bar{1}$] upon IP poling.

For both the OOP+ and the OOP− poled state, the Co film encounters a net strain ($\epsilon'_{100} - \epsilon'_{01\bar{1}}) < 0$ and the experimentally observed magnetization shows a preferred orientation close to the [100] axis in agreement with our prediction. However, in the experiment there is a 15% higher magnetization projection along the [01$\bar{1}$] axis for the OOP+ state than for the OOP− state. Since the structure of PMN-PT in the two states is equivalent, the difference has to be attributed to a contribution stemming from the FE polarization direction.

For example, the presence of interface charge σ_{int} may necessitate screening by the valence electrons of the adjacent Co film. With $2 \cdot P_{PMN-PT} = 60 \, \mu C/cm^2$, the amount of interface charge doping for fcc (111)-oriented Co can be estimated to be $\sigma_{int}(0) = \pm 0.102 \, e^-/$unit cell area. This charging will be largest at the interface and then decay exponentially corresponding to the Thomas-Fermi screening as $\sigma_{int}(z) = \sigma_{int}(0)e^{-z/\lambda_{Co}}$, where z measures the distance from the interface and λ_{Co} is the Thomas-Fermi-screening length of Co ($\lambda_{Co} = 0.15$ nm [46]).

Next we examine the impact of this interface charge on the magnetoelastic constants $[B_1(\sigma), B_2(\sigma)]$, as shown in Fig. 3(a), by repeating our computations with a varied total e^- count within the DFT calculations. We find [Fig. 3(a)] a strong variation of B_1 with charging, whereas B_2 remains nearly unchanged. Moreover, the different behavior of B_1 and
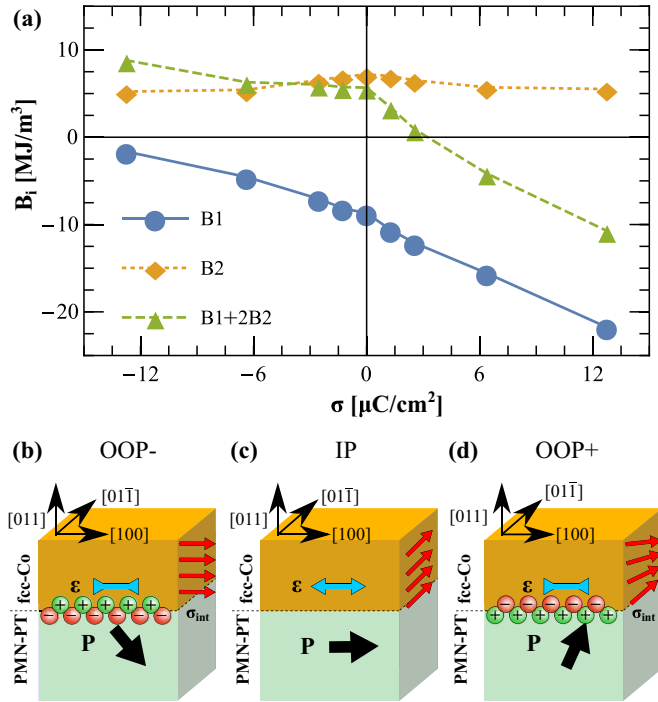
FIG. 3. (a) Variation of magnetoelastic constants as a function of charging of the unit cell σ. (b)–(d) Sketch of the three switching states (OOP−, IP, OOP+) of the Co/PMN-PT interface. The black/red arrows show the direction of electric/magnetic polarization and the blue arrows show the net strain. (b) Illustrates the OOP− case where strain and electron depletion in the Co film lead to a preference of the [100] direction as the easy axis. (c) Depicts the highly strained IP state with no interface charging and an easy axis along [01$\bar{1}$]. In (d) the combination of strain and electron accumulation creates an easy axis along [01$\bar{1}$] at the interface which decays and turns towards [100] away from the interface.

B_2 as a function of charging leads to a sign change of B_{eff} around $\sigma = 4$ μC/cm^2, as depicted by a dashed green line in Fig. 3(a). For the same negative net strain corresponding to OOP poled PMN-PT, the OOP+ and OOP− cases have different alignments of the magnetic easy axis at the interface, as sketched in Figs. 3(b) and 3(d). For the OOP− case, the accumulation of holes in the Co film at the interface ($\sigma < 0$, $B_{\text{eff}} > 0$) creates an easy axis along the [100] direction. On the other hand, in the OOP+ state the accumulation of electrons ($\sigma > 0$) reverses the sign of B_{eff} and thus favors the orthogonal [01$\bar{1}$] direction as easy magnetization direction. Consequently, we expect that switching of the electric polarization in combination with an alteration of the magnetoelastic constants by interface charging leads to a 90° change of the preferred magnetization direction. This magnetoelectroelastic effect will be constrained to the interface region, where enough charge accumulation is present.

The experimentally observed higher remanent magnetization along the [01$\bar{1}$] direction for the OOP+ state compared to the OOP− state in Figs. 1 and 2 is in agreement with our calculated magnetoelectroelastic effect. However, the detected signal contains contributions of both, the strain that extends throughout the entire film, as well as the charge—an interface effect. Consequently, the exponential decay of the charge

screening away from the Co/PMN-PT interface suppresses the measurement of this charge-enhanced effect in thicker films when using surface-sensitive TEY detection mode [Fig. 1(g)].

In conclusion, we investigated by a combined experimental and theoretical effort the room-temperature magnetoelectric properties of the Co/PMN-PT interface. From our XMCD measurements we found that the magnetic anisotropy behavior of the Co film depends on the three distinct polarization states [IP, OOP(+,−)] the PMN-PT can be set in. According to our theoretical investigation, the combination of magnetoelasticity and interface charging leads to changes in Co magnetic anisotropy, opening up the possibility for enhanced magnetoelectric coupling as well as tailoring of magnetic spin textures through the application of electric field pulses. Finally, we suggest that the found modulation of magnetic anisotropy by the magnetoelectroelastic effect allows the generation of a magnetic anisotropy gradient in thin films. If the gradient is strong enough, it gives rise to a spiral state in the thin film, which is reversible, nonvolatile, and can be controlled by the ferroelectric substrate. Our results open pathways for the exploration of new interface coupling mechanisms where different effects can be combined with the aim of enhancing or tailoring new functionalities.

APPENDIX A: EXPERIMENTAL DETAILS ON XMCD SPECTRA AND SUM RULE ANALYSIS

Regarding the XMCD spectra taken in TEY mode, the detected electron current was influenced by the respective bias voltage applied at the sample holder serving as bottom electrode [for the measurement geometry, see Fig. 1(a)]. A positive voltage on the sample holder attracts electrons that in turn leave the sample surface giving rise to a detectable TEY signal; a negative bias voltage on the sample holder prevents electrons from leaving the sample surface. To ensure a consistent electron yield background and intensity, we can apply electric field pulses to set a specific FE orientation and then measure TEY spectra with no bias voltage across the PMN-PT substrate. However, TEY spectra taken during application of large negative bias on the sample holder have vanishing intensity, making quantitative comparison
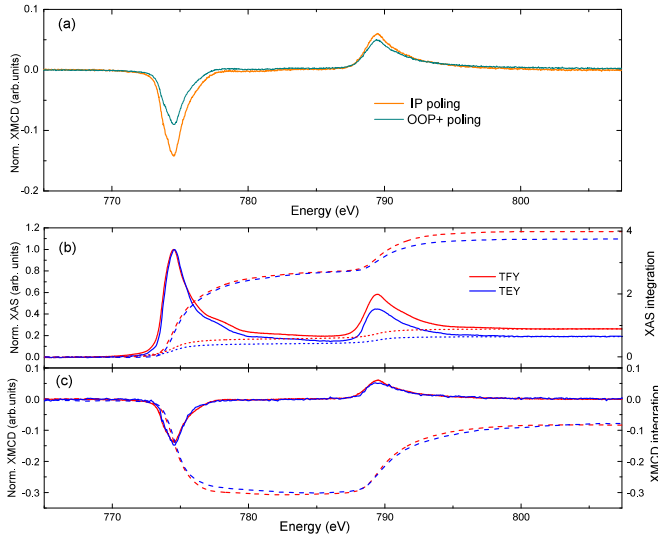
FIG. 4. (a) Example of Co XMCD difference spectra taken with TFY as a function of applied electric field. (b) and (c) Example of the sum rule analysis: (b) XAS spectra and their integration after subtraction of a two-step background resulting from TEY (blue) and TFY (red) measurements. (c) Corresponding XMCD spectra and their integration.

difficult between spectra for large negative sample holder bias.

Thus, we evaluate the electric field dependence of the total magnetic moment shown in Fig. 2 of the main text through sum rule analysis for a set of XMCD spectra taken in total fluorescence yield, as unlike electrons, the fluorescent photons are not influenced by the polarity and the strength of the applied electric field. Two examples of the detected XMCD difference as a function of applied electric field are given in Fig. 4(a), with each spectrum normalized to the XAS L_3 edge jump.

For example, we show sum rule analysis [37–39] on TEY and TFY spectra in Figs. 4(b) and 4(c) simultaneously measured in grazing incidence geometry at 0 T after saturation in a magnetic field of 2 T and in an applied electric field of -0.14 MV/m (IP poled state) at a nominal Co thickness of 3.5 nm. In this figure the XAS is defined as the sum of x-ray absorption spectra measured with left and right circular polarization, while the XMCD is the difference between these spectra. For the analysis, an electron occupation number of 7.51 was used for cobalt [39]. Our DFT calculations show that the magnetic dipole term T_z is on the order of $\langle T_z \rangle = 1.4 \times 10^{-3} \mu_B$ and therefore negligible. Figure 4(b) shows XAS spectra taken with TEY (blue) and TFY (red). The integration of each XAS spectrum (dashed curve) after subtraction of a two-step background function is also shown in the respective color. Figure 4(c) shows the XMCD spectra and their integration resulting from TEY (blue) and TFY (red) measurements. The total magnetic moment extracted from the TEY spectrum sums up to $m_{tot} = 1.23 \mu_B$, m_{tot} extracted from the TFY spectrum is $m_{tot} = 1.16 \mu_B$. Comparison of the TEY and TFY spectra shows that the sum rules analysis of the latter results in an about 6% smaller total magnetic moment value.

The error bar in the sum rule analysis among the set of TFY spectra as determined from the spectra quality is estimated to be 3.5%.

For completeness we give the orbital moments deduced for Co on PMN-PT for the three distinct poling states. The orbital moment is very small compared to the effective spin moment, with $m_{orb} = 0.065 \pm 0.005 \mu_B$ for OOP+ poled PMN-PT, $m_{orb} = 0.045 \pm 0.007 \mu_B$ for OOP$-$ poled PMN-PT, and $m_{orb} = 0.079 \pm 0.013 \mu_B$ for IP poling.

The TEY hysteresis curves shown in Fig. 1 were measured at the Advanced Light Source using a positively biased grid in front of the sample holder to minimize any influence due to an applied voltage across the PMN-PT substrate.

APPENDIX B: TRANSFORMATION OF MAGNETOELASTIC ENERGY

The transformation of the magnetoelastic energy for the case of a (111)-oriented film, has been performed by utilizing the transformation matrix [43]:

$$\overline{a} = \begin{pmatrix} -\frac{1}{\sqrt{2}} & \frac{1}{\sqrt{2}} & 0 \\ -\frac{1}{\sqrt{6}} & -\frac{1}{\sqrt{6}} & \sqrt{\frac{2}{3}} \\ \frac{1}{\sqrt{3}} & \frac{1}{\sqrt{3}} & \frac{1}{\sqrt{3}} \end{pmatrix}. \quad (B1)$$

The strain tensor in the cubic coordinate system of PMN-PT substrate is

$$\overline{\epsilon}' = \begin{pmatrix} \epsilon'_{101} & 0 & 0 \\ 0 & \epsilon'_{0\overline{1}1} & 0 \\ 0 & 0 & \epsilon'_{011} \end{pmatrix}, \quad (B2)$$

which transforms as

$$\overline{\epsilon} = \overline{a}^T \overline{\epsilon}' \, \overline{a}. \quad (B3)$$

Finally, we use $\overline{\epsilon}$ in Eq. (4) to determine the easy axis within the film plane.

APPENDIX C: CALCULATION OF MAGNETOELASTIC COEFFICIENTS

To calculate the magnetoelastic constants we map the DFT total energy onto the phenomenological expression for the cubic magnetoelastic energy:

$$E_{ME}(\boldsymbol{\alpha}, \overline{\epsilon}) = B_1 \left(\epsilon_{11} \alpha_1^2 + 2\epsilon_{22}\alpha_2^2 + \epsilon_{33}\alpha_3^2 \right)$$
$$+ 2B_2 (\epsilon_{23}\alpha_2\alpha_3 + \epsilon_{13}\alpha_1\alpha_3 + \epsilon_{12}\alpha_1\alpha_2), \quad (C1)$$

where α_i is the direction cosine, ϵ_{ij} is the transformed strain tensor components as described in the previous section, and B_i is the magnetoelastic constants. The two magnetoelastic coefficients are then computed by two sets of calculations. For B_1 we apply a strain ϵ_{11} and compute the energies $E_{[100]}$ and $E_{[001]}$ for magnetizations along the [100] ($\alpha_1 = 1, \alpha_2 = \alpha_3 = 0$) and [001] ($\alpha_1 = \alpha_2 = 0, \alpha_3 = 1$) directions, respectively. B_1 is then given by

$$B_1 = \frac{E_{[100]} - E_{[001]}}{\epsilon_{11}}. \quad (C2)$$

The procedure for B_2 is similar, where we strain the cell corresponding to $\epsilon_{23} \neq 0$ and calculate the energies $E_{[011]}$ and

$E_{[01\bar{1}]}$ for magnetizations along [011] $\alpha_2 = \alpha_3 = \frac{1}{\sqrt{2}}$ and [01$\bar{1}$] $\alpha_2 = -\alpha_3 = \frac{1}{\sqrt{2}}$, respectively. Again one finds

$$B_2 = \frac{E_{[011]} - E_{[01\bar{1}]}}{2\epsilon_{23}}. \quad (C3)$$

Both magnetoelastic constants are computed from total energy calculations performed within density-functional theory using the projector augmented wave PAW [47] method as implemented in the Vienna *ab initio* simulation package [48]. For the exchange-correlation potential we utilized the generalized gradient approximation (PBE) [49], where our

selected pseudopotential for Co contains 17 valence electrons corresponding to the electronic configuration $3s^2 3p^6 3d^7 4s^2$. For the self-consistent calculations we use 800 eV as the cutoff energy for the plane wave expansion and a $45 \times 45 \times 45$ Monkhorst-Pack grid for sampling the Brillouin zone of the cubic fcc cell containing four atoms. Finally, we calculate the needed energy differences by performing non-self-consistent calculations for different magnetization directions with an increased sampling of $90 \times 90 \times 90$ k points. All numerical parameters have been thoroughly tested to give consistent results in the energy range of magnetoelastic energies (10^{-8} eV).

[1] S. Stemmer and S. James Allen, Annu. Rev. Mater. Res. **44**, 151 (2014).

[2] J. Nogués and I. K. Schultz, J. Magn. Magn. Mater. **192**, 203 (1999).

[3] M. Weisheit, S. Fahler, A. Marty, Y. Souche, C. Poinsignon, and D. Givord, Science **315**, 349 (2007).

[4] J. M. Rondinelli, M. Stengel, and N. A. Spaldin, Nat. Nanotechnol. **3**, 46 (2007).

[5] T. Maruyama, Y. Shiota, T. Nozaki, K. Ohta, N. Toda, M. Mizuguchi, A. A. Tulapurkar, T. Shinjo, M. Shiraishi, S. Mizukami, Y. Ando, and Y. Suzuki, Nat. Nanotechnol. **4**, 158 (2009).

[6] R. Ramesh and N. A. Spaldin, Nature (London) **6**, 21 (2007).

[7] G. Srinivasan, E. T. Rasmussen, B. J. Levin, and R. Hayes, Phys. Rev. B **65**, 134402 (2002).

[8] W. Eerenstein, M. Wiora, J. L. Prieto, J. F. Scott, and N. D. Mathur, Nat. Mater. **6**, 348 (2007).

[9] C. Thiele, K. Dörr, O. Bilani, J. Rödel, and L. Schultz, Phys. Rev. B **75**, 054408 (2007).

[10] J. J. Yang, Y. G. Zhao, H. F. Tian, L. B. Luo, H. Y. Zhang, Y. J. He, and H. S. Luo, Appl. Phys. Lett. **94**, 212504 (2009).

[11] T. Wu, A. Bur, P. Zhao, K. P. Mohanchandra, K. Wong, K. L. Wang, C. S. Lynch, and G. P. Carman, Appl. Phys. Lett. **98**, 012504 (2011).

[12] R. V. Chopdekar, V. K. Malik, A. Fraile-Rodríguez, L. Le Guyader, Y. Takamura, A. Scholl, D. Stender, C. W. Schneider, C. Bernhard, F. Nolting, and L. J. Heyderman, Phys. Rev. B **86**, 014408 (2012).

[13] S. Zhang, Y. G. Zhao, P. S. Li, J. J. Yang, S. Rizwan, J. X. Zhang, J. Seidel, T. L. Qu, Y. J. Yang, Z. L. Luo, Q. He, T. Zou, Q. P. Chen, J. W. Wang, L. F. Yang, Y. Sun, Y. Z. Wu, X. Xiao, X. F. Jin, J. Huang, C. Gao, X. F. Han, and R. Ramesh, Phys. Rev. Lett. **108**, 137203 (2012).

[14] J. Heidler, C. Piamonteze, R. V. Chopdekar, M. A. Uribe-Laverde, A. Alberca, M. Buzzi, A. Uldry, B. Delley, C. Bernhard, and F. Nolting, Phys. Rev. B **91**, 024406 (2015).

[15] C. A. F. Vaz, J. Hoffman, Y. Segal, J. W. Reiner, R. D. Grober, Z. Zhang, C. H. Ahn, and F. J. Walker, Phys. Rev. Lett. **104**, 127202 (2010).

[16] D. Yi, J. Liu, S. Okamoto, S. Jagannatha, Y.-C. Chen, P. Yu, Y.-H. Chu, E. Arenholz, and R. Ramesh, Phys. Rev. Lett. **111**, 127601 (2013).

[17] D. Preziosi, M. Alexe, D. Hesse, and M. Salluzzo, Phys. Rev. Lett. **115**, 157401 (2015).

[18] M. Fechner, P. Zahn, S. Ostanin, M. Bibes, and I. Mertig, Phys. Rev. Lett. **108**, 197206 (2012).

[19] G. Radaelli, D. Petti, E. Plekhanov, I. Fina, P. Torelli, B. R. Salles, M. Cantoni, C. Rinaldi, D. Gutiérrez, G. Panaccione, M. Varela, S. Picozzi, J. Fontcuberta, and R. Bertacco, Nat. Commun. **5**, 1 (2014).

[20] H. Béa, M. Bibes, F. Ott, B. Dupé, X. H. Zhu, S. Petit, S. Fusil, C. Deranlot, K. Bouzehouane, and A. Barthélémy, Phys. Rev. Lett. **100**, 017204 (2008).

[21] S. M. Wu, S. A. Cybart, P. Yu, M. D. Rossell, J. X. Zhang, R. Ramesh, and R. C. Dynes, Nat. Mater. **9**, 756 (2010).

[22] K. J. A. Franke, B. van de Wiele, Y. Shirahata, S. J. Hämäläinen, T. Taniyama, and S. van Dijken, Phys. Rev. X **5**, 011010 (2015).

[23] M. Gajek, M. Bibes, S. Fusil, K. Bouzehouane, J. Fontcuberta, A. Barthélémy, and A. Fert, Nat. Mater. **6**, 296 (2007).

[24] V. Garcia, M. Bibes, L. Bocher, S. Valencia, F. Kronast, A. Crassous, X. Moya, S. Enouz-Vedrenne, A. Gloter, D. Imhoff, C. Deranlot, N. D. Mathur, S. Fusil, K. Bouzehouane, and A. Barthélémy, Science **327**, 1106 (2010).

[25] S. Valencia, A. Crassous, L. Bocher, V. Garcia, X. Moya, R. O. Cherifi, C. Deranlot, K. Bouzehouane, S. Fusil, A. Zobelli, A. Gloter, N. D. Mathur, A. Gaupp, R. Abrudan, F. Radu, A. Barthelemy, and M. Bibes, Nat. Mater. **10**, 753 (2011).

[26] D. Pantel, S. Goetze, and M. Alexe, Nat. Mater. **11**, 289 (2012).

[27] J.-M. Hu, C.-W. Nan, and L.-Q. Chen, Phys. Rev. B **83**, 134408 (2011).

[28] L. Shu, Z. Li, J. Ma, Y. Gao, L. Gu, Y. Shen, Y. Lin, and C. W. Nan, Appl. Phys. Lett. **100**, 022405 (2012).

[29] T. Nan, Z. Zhou, M. Liu, X. Yang, Y. Gao, B. A. Assaf, H. Lin, S. Velu, X. Wang, H. Luo, J. Chen, S. Akhtar, E. Hu, R. Rajiv, K. Krishnan, S. Sreedhar, D. Heiman, B. M. Howe, G. J. Brown, and N. X. Sun, Sci. Rep. **4**, 3688 (2014).

[30] N. A. Pertsev, Phys. Rev. B **92**, 014416 (2015).

[31] B. Noheda, D. E. Cox, G. Shirane, J. Gao, and Z. G. Ye, Phys. Rev. B **66**, 054104 (2002).

[32] X-ray diffraction reciprocal space maps on (011)-oriented PMN-PT show that switching to an IP poled state is accompanied by a tensile lattice parameter change of +0.90% along the [100] direction, as well as compressive lattice parameter changes of −0.23% along the [01$\bar{1}$] and −0.70% along the [011] direction, exerting strain on the Co layer.

[33] C. Piamonteze, U. Flechsig, S. Rusponi, J. Dreiser, J. Heidler, M. Schmidt, R. Wetter, M. Calvi, T. Schmidt, H. Pruchova,

J. Krempasky, C. Quitmann, H. Brune, and F. Nolting, J. Synchrotron Radiat. **19**, 661 (2012).

[34] P. Nachimuthu, J. H. Underwood, C. D. Kemp, E. M. Gullikson, D. W. Lindle, D. K. Shuh, and R. C. C. Perera, in *Synchrotron Radiation Instrumentation: Eighth International Conference on Synchrotron Radiation Instrumentation* (AIP, New York, 2004), pp. 454–457.

[35] J. Stöhr and H. C. Siegmann, *Magnetism: From Fundamentals to Nanoscale Dynamics*, edited by M. Cardona, P. Fulde, K. von Klitzing, R. Merilin, H. J. Queisser, and H. Störmer, Solid-State Sciences, Vol. 152 (Springer, New York, 2006).

[36] R. Nakajima, J. Stöhr, and Y. U. Idzerda, Phys. Rev. B **59**, 6421 (1999).

[37] B. T. Thole, P. Carra, F. Sette, and G. van der Laan, Phys. Rev. Lett. **68**, 1943 (1992).

[38] P. Carra, B. T. Thole, M. Altarelli, and X. Wang, Phys. Rev. Lett. **70**, 694 (1993).

[39] C. T. Chen, Y. U. Idzerda, H. J. Lin, N. V. Smith, G. Meigs, E. Chaban, G. H. Ho, E. Pellegrin, and F. Sette, Phys. Rev. Lett. **75**, 152 (1995).

[40] M. Tischer, O. Hjortstam, D. Arvanitis, J. H. Dunn, F. May, K. Baberschke, J. Trygg, J. M. Wills, B. Johansson, and O. Eriksson, Phys. Rev. Lett. **75**, 1602 (1995).

[41] P. Bruno, J. Phys. F **18**, 1291 (1988).

[42] C. Chappert and P. Bruno, J. Appl. Phys. **64**, 5736 (1988).

[43] D. Sander, Rep. Prog. Phys. **62**, 809 (1999).

[44] G. Y. Guo, D. J. Roberts, and G. A. Gehring, Phys. Rev. B **59**, 14466 (1999).

[45] M. Komelj and M. Fähnle, J. Magn. Magn. Mater. **224**, 1 (2001).

[46] S. Zhang, Phys. Rev. Lett. **83**, 640 (1999).

[47] P. E. Blöchl, Phys. Rev. B **50**, 17953 (1994).

[48] G. Kresse and J. Furthmüller, Phys. Rev. B **54**, 11169 (1996).

[49] J. P. Perdew, K. Burke, and M. Ernzerhof, Phys. Rev. Lett. **77**, 3865 (1996).